THE JOURNAL OF Ammonia Energy

Available online at

jae.cardiffuniversitypress.org

ISSN **2752-7735**
The Journal of Ammonia Energy 01 (2023) 106–117

Cardiff University Press | Gwasg Prifysgol Caerdydd

Investigation of NO Production and Flame Structures in Ammonia-Hydrogen Flames

Cosway B*, Ahmed P, Talibi M*, Balachandran R
University College London, Torrington Place, London, WC1E 7JE, United Kingdom

Abstract
Ammonia/hydrogen fuel blends have recently emerged as a promising solution to the de-carbonization of the energy and transport sectors. However, concerns over performance and, more importantly, NOx emissions have impeded their progress so far. Before effective NOx mitigation strategies can be developed, the fundamental chemical mechanisms involved in NOx production in NH_3/H_2 flames must be well understood. Although NOx formation in hydrocarbons and the oxidative processes involved in NH_3 combustion have been well studied, there is a significant lack of such information for NH_3/H_2 flames. Key insights on NO formation mechanisms and flame structures for NH_3/H_2 mixtures are required to develop and improve chemical kinetic models. In this work, laminar Bunsen NH_3/H_2 flames with 65/35 NH_3/H_2 volume fraction were tested at two equivalence ratios (rich and lean). For all test conditions, the adiabatic flame temperature was kept constant. Measurements of simultaneous OH/NO-PLIF and OH-PLIF/chemiluminescence (of NH*, NH_2* and OH*) were conducted and compared to computational results of four reaction mechanisms (available in literature) applicable to NH_3/H_2 flames. The maximum OH-PLIF signal gradient was used as a spatial reference point for each simultaneous measurement and one-dimensional line profiles were determined for each species of interest. The simultaneous OH/NO-PLIF images show that the NO signal intensity in the NH_3/H_2 flames were up to 100 times more than a CH_4 reference flame. OH* and NH* chemiluminescence results showed a good spatial correlation with the maximum OH-PLIF signal gradient for both test conditions. NH* also showed a positive correlation with the computed HRR values from lean to rich, indicating it is a promising candidate for direct HRR measurement but warrants further investigation over a wide range of equivalence and mixture ratios. The results also indicate that all the mechanisms underestimate the profile widths of the measured species. Similarly, the experimental results showed a much higher relative increase in NH_2 production from lean to rich compared to the computed profiles. The data analysis approach employed in this paper, based on simultaneous measurements, could be further used for optimizing chemical kinetics mechanisms for NH_3/H_2 flames.

Received: 7th April 23; Accepted: 12th June 23; Published: 4th July 23

Keywords: Ammonia hydrogen flames, Laser Diagnostics, NO, Laminar flames, Chemical kinetics

Introduction
In recent years, ammonia has gained significant interest for its use as a carbon free energy carrier [1]. However, there are many challenges associated with using NH_3 as a fuel, such as flame stabilisation and high NO_x production during combustion, due to its relatively low flame speed/reactivity and fuel bound nitrogen respectively. These are the main issues that have hindered its deployment in full-scale commercial energy systems to date. Addition of hydrogen to ammonia has been shown to increase flame stability, due to its high reactivity, however this can also lead to increased flame temperatures and thus increased NO_x emissions [2–13]. In certain ratios, ammonia/hydrogen blends have been shown to exhibit very similar properties to current hydrocarbon fuels which makes them an excellent solution for the de-carbonisation of power generation and transport [6–8]. However, the increased level of NO_x emissions produced during the combustion of these fuel blends needs to be limited to an acceptable level for them to become a reality.

Various experimental and computational studies have been conducted characterising NO formation in NH_3/H_2 flames, for a range of mixture compositions. Zhu et al. have shown that super lean conditions ($\Phi \approx 0.4$) can result in low NO_x emissions (down to 100 ppm) for a range of mixture fractions (50-80 % vol. NH_3) in a laboratory scale swirl burner [14]. Valera-Medina et al. have shown that a mixture of 70/30 (v/v) NH_3/H_2 under rich conditions also provides stable combustion in a gas turbine swirl burner [6]. They provided complementary computational analysis showing that hot unburned NH_3 could be used for further reaction with existing

* Corresponding authors. E-mail address: benjamin.cosway.19@.ucl.ac.uk, m.talibi@ucl.ac.uk
https://doi.org/10.18573/jae.20

NO_x, reducing it to relatively low levels (<50ppm). However, this was achieved at reduced efficiencies compared to current DLN (dry low NO_x) technologies. Similarly, Hussain et al. simulated rich NH_3/H_2 flames (Φ=1.2) in a swirl burner, but came to the conclusion that a 60/40 (v/v) blend showed the least unburned ammonia and highest flame temperatures [3, 13]. They also showed that the NO_x formed due to the higher temperatures could be abated by injecting a small amount of the NH_3/H_2 fuel downstream of the reaction zone. Mashruk et al. investigated premixed NH_3/H_2 blends at different volumetric ratios with different thermal powers and Reynolds numbers at a fixed lean equivalence ratio (Φ=0.65) [15]. They found that, at this industrially representative equivalence ratio (for Dry Low NO_x technologies), there was possibility of high N_2O emissions. Reaction pathway analyses showed that this was primarily due to NO consumption with NH, which increases with increasing ammonia content in the fuel. Overall, it is clear that there is a trade-off between efficiency, stability and reduction of the different NO_x constituents to achieve results close to that of current hydrocarbon fuels.

As for computational work, focused on developing and understanding the reaction mechanisms involved with NH_3/H_2 combustion, there are only a handful of studies that have explicitly included H_2 in their validation experiments and subsequent reaction mechanisms. Although, pure NH_3 models already include the sub-mechanism for H_2, so have also been used by some authors. The mechanism presented by Otomo et al. [10] was based on one that was developed by Song et al. [16] for ammonia oxidation at high pressure (30 bar and 100 bar) and intermediate temperatures (450-925 K), but with an improved reaction mechanism for NH_3/H_2/air combustion. However, the authors provided no additional experimental data to validate their improvements. On the other hand, the mechanism developed by Mei et al. [17] was validated by laminar burning velocity experiments of different NH_3/H_2 ratios and equivalence ratios. The mechanism itself was based on their previous NH_3/syngas mechanism [18] but updated to include H_2 addition. The mechanism by Stagni et al. [19] was developed for pure ammonia, however they included jet-stirred reactor and flow reactor experiments in their study, producing comprehensive data on product and intermediate formation. Furthermore, this mechanism has also shown good correlation to experimental results for NO production in premixed NH_3/H_2 swirling flames previously [15]. Similarly, Zhang et al. [4] used jet-stirred reactor experiments for mechanism validation, however they also included different levels of hydrogen addition from zero to 70%. This mechanism was also largely based off the mechanism produced by Mei et al. It can be seen from literature that the most reliable models are those which are optimised using species formation data, from jet-stirred reactors, as opposed to global parameters like laminar flame speeds and ignition delay times, as it provides more information regarding the reaction pathways and formation rates of the different species.

In terms of measuring NO_x formation in flames, various intrusive and non-intrusive methods can be employed. Intrusive methods such as gas sampling can provide accurate quantitative measurements of NO_x gases but cannot provide spatial data unless complex scanning techniques are used. Regardless, these sampling techniques will result in physical alterations to the flame itself. On the other hand, non-intrusive, optical based techniques do not affect the flame structure and provide highly spectrally and temporally resolved data. NO Planer Laser-Induced Fluorescence (PLIF) is an advanced laser diagnostic technique that has been used to provide detailed information on the spatial and temporal distribution of NO concentrations in different flames in numerous different studies [20–26]. As it is the main component of NO_x, directly measuring the spatial variation of NO intensity is extremely important for understanding NO_x formation chemistry and subsequently developing reduction techniques.

As well as directly measuring NO signal intensities, it is important to investigate how the flame structure affects NO_x production. The heat release rate (HRR) is a fundamental property of combustion processes, characterizing the extent of energy conversion from chemical to thermal and thus dictating the flame structure. The spatial distribution of the HRR can provide locations of reaction zones [27], which allows for the spatial comparison of species concentrations. Due to the difficulty in obtaining HRR measurements directly, indirect methods such as LIF and chemiluminescence of different surrogate species are often used. The most common method of HRR measurement in hydrocarbon flames is the product of both [OH] and [CH2O] [28] (here [] indicates PLIF signal levels). OH* chemiluminescence has also been shown to provide a strong linear correlation to HRR in premixed methane-air flames [29]. $[NH_3]$x[OH], $[NH_2]$x[O], and $[NH_2]$x[H] have all been proposed as potential HRR markers for NH_3 flames, however their suitability varied with equivalence ratio [30]. As for NH_3/H_2 flames specifically, [OH] gradient and [NH] have been computationally shown to be suitable for a wide range of conditions [12]. However, there is a distinct lack of comparison between experimental markers and computed HRR. In terms of intermediate species measurements, which form the main structure of the flame and influence NO

production, various spectroscopic methods can be used [31]. The chemiluminescence spectrum in ammonia flames consists of NO*, OH*, and NH* radicals in the UV range and the NH_2* radicals in the visible range [14], all of which have successfully been imaged in previous studies in NH_3/H_2 flames [14, 15].

In order to develop robust NO_x mitigation strategies for ammonia/hydrogen fuels, the fundamental NOx formation mechanisms must be well understood. NO_x formation in hydrocarbon combustion has been extensively studied and is well understood [32, 33]. However, as can be seen from the literature review above, the mechanisms differ for ammonia/hydrogen combustion due to the presence of fuel bound nitrogen and absence of carbon. The oxidative processes involved in ammonia breakdown are well defined, due to its use in selective non-catalytic reduction of NO_x [34]. However, the applicability of these processes to NO_x production and the addition of H_2 requires further development [2, 35].

The above review highlights the lack of experimental data in literature on the spatial distribution of NO and intermediate species in laminar NH_3/H_2 flames. This work aims to address this gap, and furthermore investigates chemiluminescence flame markers that are representative of the heat release rate. The experimental results were compared to computations of 1-D freely propagating NH_3/H_2 flames using four relevant chemical mechanisms. Slightly lean and rich equivalence ratios for a NH_3/H_2 ratio of 65/35 (v/v) were investigated using a premixed laminar Bunsen flame. This approach allowed the adiabatic flame temperature to be kept constant to exclude thermal effects on NO production. Simultaneous PLIF of OH/NO and OH-PLIF/chemiluminescence measurements of OH*, NH* and NH_2* were conducted. OH-PLIF was measured simultaneously to be used as a spatial reference point between flames and different species measurements, as well as being assessed as a HRR marker in its own right, as recommended by Zhang et al. [11]. This fundamental analysis will provide useful and novel insights for both the experimental and modelling communities with regards to the combustion of NH_3/H_2 mixtures, aiming to contribute to their understanding and adoption as carbon-free fuels.

Materials and Methods

A simple premixed Bunsen burner arrangement was used to stabilise the NH_3/H_2 flames, under room temperature and pressure conditions, with varying equivalence ratio and NH_3/H_2 ratio. The Bunsen burner consisted of a steel tube, of 500 mm in length, with an inner diameter of 10 mm. Mass flow meters were used for air (Vogtlin) and hydrogen (Bronkhorst) and a rotameter (Roxspur) was used for ammonia to control the reactant flow to the burner. The details of the experimental conditions are shown in Table 1. The NH_3/H_2 mixture chosen for investigation was 65/35 (v/v). Two different flames at this ratio were investigated, with slightly rich and slightly lean equivalence ratios along with a reference methane flame for comparison (Also shown in Table 1). Adiabatic flame temperatures (±5K) and bulk velocities (±0.05m/s) were kept constant to avoid global temperature effects on species production, so that trends would be purely based on the respective fuel composition being investigated.

Simultaneous PLIF of OH/NO and OH-PLIF/chemiluminescence measurements were conducted on the laminar Bunsen NH_3/H_2 flames. For the NO-PLIF laser arrangement, a 10Hz Nd:YAG laser (Litron, LPY7864G-10) was used to pump a tunable dye laser (LiopTec, LiopStar-E) which was then frequency tripled to obtain a wavelength of around 226 nm, to excite the A-X(0,0) band of NO. The specific rotational transition targeted was the P1(23.5) (and neighbouring bands) at 226.03 nm (≈225.96nm in air). The energy output was approximately 2.4 mJ per pulse. NO fluorescence from the A-X(0,2) and A-X(0,3) vibrational bands were detected using an ICCD (PIMAX 4, Princeton Instruments) with a sensor size of 1024 x 1024 and a projected pixel resolution of 41.7 μm. It was equipped with a 45mm UV lens (F1.8 CERCO 2073, Sodern) and a combination of 265 nm and 325 nm shortpass filters (Asahi

Table. 1. Running conditions for the laminar NH_3/H_2 flames and reference laminar CH_4 flame.

NH_3 %	H_2 %	Φ	T_{ad} (K)	NH_3 Flow Rate (sl/m)	H_2 Flow Rate (sl/m)	Air Flow Rate (sl/m)	Bulk Velocity (m/s)
65	35	0.973	2145.5	0.4	0.215	1.994	0.554
65	35	1.07	2147.8	0.5	0.267	2.267	0.644
CH_4 %		**Φ**	**T_{ad} (K)**	**CH4 Flow Rate (sl/m)**		**Air Flow Rate (sl/m)**	**Bulk Velocity (m/s)**
100		0.911	2148.4	0.247		2.58	0.6

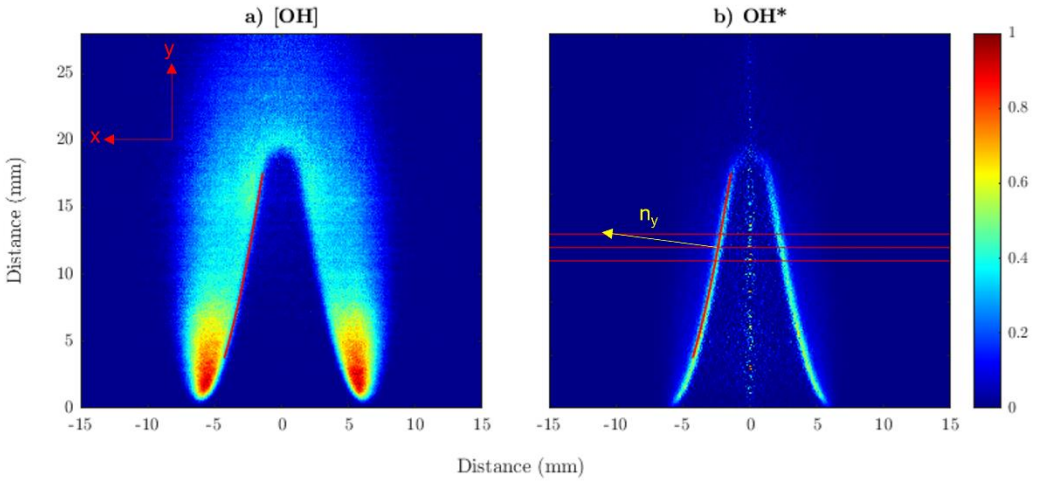

Fig. 1. OH-PLIF (a) and Abel-inverted OH* chemiluminescence (b) images of the lean 65/35 (v/v) NH_3/H_2 flame. The red curved line indicates the flame front and the three horizontal red lines represent the bounds for profile averaging, with the middle line indicating the extraction height. Both images use the flame centre as the zero-reference point here.

Spectra). OH-PLIF was conducted using a similar arrangement laser arrangement; a Nd:YAG laser (Litron, NANO- L-200-10 PIV) pumped a dye laser (LiopTec, LiopStar-E) which was frequency doubled to deliver 283 nm at approximately 8.5 mJ per pulse. This was used to excite the A-X(1,0) band of OH. The OH fluorescence near 310 nm was collected with an intensifier (VS4-1845, Videoscope) and CCD (Sensicam, PCO Imaging) with a sensor size 1024 x 1376 and a projected pixel resolution 38.5 µm. It was fitted with a 100mm UV lens and a combination of UG11 and WG305 Schott glass filters.

The two laser sheets for OH-PLIF and NO-PLIF, ≈0.2 mm thick and 50 mm in height, were counter propagated and passed through the centre of the burner at a slight angle (<1°) to avoid the risk of entering the opposing dye laser cavity. The two parallel laser sheets were time delayed by 10 µs to avoid any interference between signals and image captures. OH*, NH* and NH_2* chemiluminescence was captured on the same ICCD used for NO-PLIF (PIMAX 4, Princeton Instruments) using filters centred at 310, 355 and 632 nm respectively, with 10 nm FWHM (Edmund Optics). Intensifier gain and gate widths were adjusted to achieve a good signal-to-noise ratio whilst avoiding over-saturation of the CCD.

Image Processing

Various processing steps of the PLIF and chemiluminescence images were needed before the experimental and computational results could be compared. Due to differences in planar and line-of-sight imaging of the PLIF and chemiluminescence respectively, all the chemiluminescence images were Abel inverted to achieve a planar equivalent. 1-D line profiles of each species were then extracted using the procedure outlined below.

An average of 200 shots were taken for all the PLIF and chemiluminescence images, which were then background corrected. In order to overlap the two different fields of view (FOV) of simultaneous OH-PLIF and NO-PLIF/chemiluminescence measurements and to obtain the same pixel resolution, image warping was performed. Images of a common target were taken on each camera, and a specific image transformation from the OH-PLIF camera to the NO-PLIF/chemiluminescence camera was obtained using in-house MATLAB scripts. This was then applied to all averaged OH-PLIF images.

A two-dimensional Abel inversion of the chemiluminescence images were performed using the 3-point methodology presented in [36] and implemented by [37]. Figure 1a shows the final warped OH-PLIF image and Fig. 1b shows the corresponding simultaneous Abel inverted OH* chemiluminescence image for the lean 65/35 (v/v) NH_3/H_2 flame.

The simultaneous OH-PLIF images were used for spatial referencing by taking maximum [OH] gradient as the flame front. Firstly, a threshold was applied and an approximate 1st flame front line acquired using edge detection in the region of interest. Then, the points of maximum [OH] gradient along the normals to the 1st flame front line at each y position were found. The final flame front line is thus a polynomial fit of all of the maximum [OH] gradient points, shown as the red curves in Figs. 1a

and 1b. After the flame front line is transposed onto its simultaneous NO-PLIF/chemiluminescence image (example shown in Fig. 1b), the pixel intensities along the normal (n_y) to the flame front line at a given y position, are taken as the 1-D line profile. The limits of these profiles were +/- 1.5mm from the flame front line, in the burnt gas direction. Each final line profile is the fitted average of all the 1-D line profiles ±1mm from the extraction height (in y direction), which were 12 and 14 mm from the burner tip for the lean and rich flames respectively.

All NO-PLIF images were also corrected for spatial variations in the laser sheet. This was achieved by seeding a cold flow of NO gas (diluted in N_2 – 500 ppm) through the burner and performing NO-PLIF, using the same procedure as the flame test cases. A similar methodology was also employed for OH-PLIF laser sheet correction by seeding a flow of acetone vapour. Assuming a uniform jet out of the burner and minimal expansion, this results in a good representation of the variation in laser intensity in the vertical axis, which is then applied to the respective NO and OH-PLIF images.

Computational Modelling

One-dimensional freely propagating NH_3/H_2 flames were simulated using COSILAB [38] based on the laminar Bunsen flames presented here. 1-D analysis has been shown to provide a good approximation for conical flame surfaces [22, 27], so it was used as a benchmark to compare the experimental results presented to different current kinetic mechanisms used for NH_3/H_2 flames. The profile extraction height for each flame was chosen to minimise any stretch and curvature effects. Four different mechanisms were used for comparison that have been specifically developed for and/or previously used to evaluate NH_3/H_2 flame structures and species formation, the Stagni mechanism [19], the Otomo mechanism [10], the Mei mechanism [17] and the Zhang mechanism [4]. 1-D species formation profiles through the flame reaction zone were calculated for each flame condition using each mechanism and yielded valuable comparisons between each other and the experimental 1-D profiles.

Results

The results are presented in three different sections. As the main focus of this study is the investigation of the spatial formation of NO in NH_3/H_2 flames, the first section focuses solely on the NO PLIF results, their line profiles and their comparison to the computed line profile results from each of the four aforementioned mechanisms. The second section focuses on the chemiluminescence line profile results for NH* and NH_2* and their comparison to the computed line profile results as well as how they influence the production of NO. The final section evaluates the suitability of the chemiluminescence line profiles of OH* and NH*, as well as [OH] gradient, as HRR markers by comparing to the computed HRR profiles from each mechanism.

For the experimental results, the 1D line profiles presented here constitute the averaged pixel intensities from the normals to the flame front around the given extraction height, discussed in section 2.1. For the computational results the 1D line profiles constitute the computed mole fractions by each mechanism in the same spatial domain (using the same set parameters and numerical method for each). The alignment of the NO and chemiluminescence profiles are based on their respective simultaneous [OH] flame front lines as the zero-reference point (maximum [OH] gradient). The computed profiles are based on their respective point of maximum HRR as the zero-reference point. All presented profiles are normalized using their respective lean case maximum to allow for comparison between equivalence ratios and the experimental and computational results.

NO Formation Characteristics

Figure 2 shows the processed simultaneous OH and NO PLIF images for the (a) lean and (b) rich 65/35 (v/v) NH_3/H_2 flames, as well as the (c) lean CH_4 reference flame. Firstly, comparing the NO signal intensity levels of the NH_3/H_2 flames to CH_4, it can be seen that the signal intensity is up to 100 times higher. The much higher NO signal in the ammonia flames, despite having the same adiabatic flame temperatures, could be attributed to the fuel bound nitrogen in the ammonia. The breakdown of ammonia into NH_i and subsequent oxidation into HNO is the primary pathway for NO formation in ammonia flames [1]. This can help explain the differences in the spatial variation of [NO] signal level shown in Fig. 2 between NH_3/H_2 and CH_4. In CH4 flames NO_x formation is primarily through the thermal mechanism which, due to its high temperature dependence, will tend to occur above the flame tip in the hot post-flame gases [30]. In NH_3/H_2 flames, however, the fuel-NO pathway is dominant and results in the formation of NO around the flame front region as the NH_3 starts to break down before the peak temperatures are reached after the flame front.

Now comparing the rich and lean cases for NH_3/H_2 flames (Figs. 2a and 2b), the [NO] signal intensity in the lean NH_3/H_2 flame is generally much higher than the rich and more spatially uniform downstream of the flame front. Also, in the rich flame there is a much higher concentration around the points of curvature. These observations could be explained by

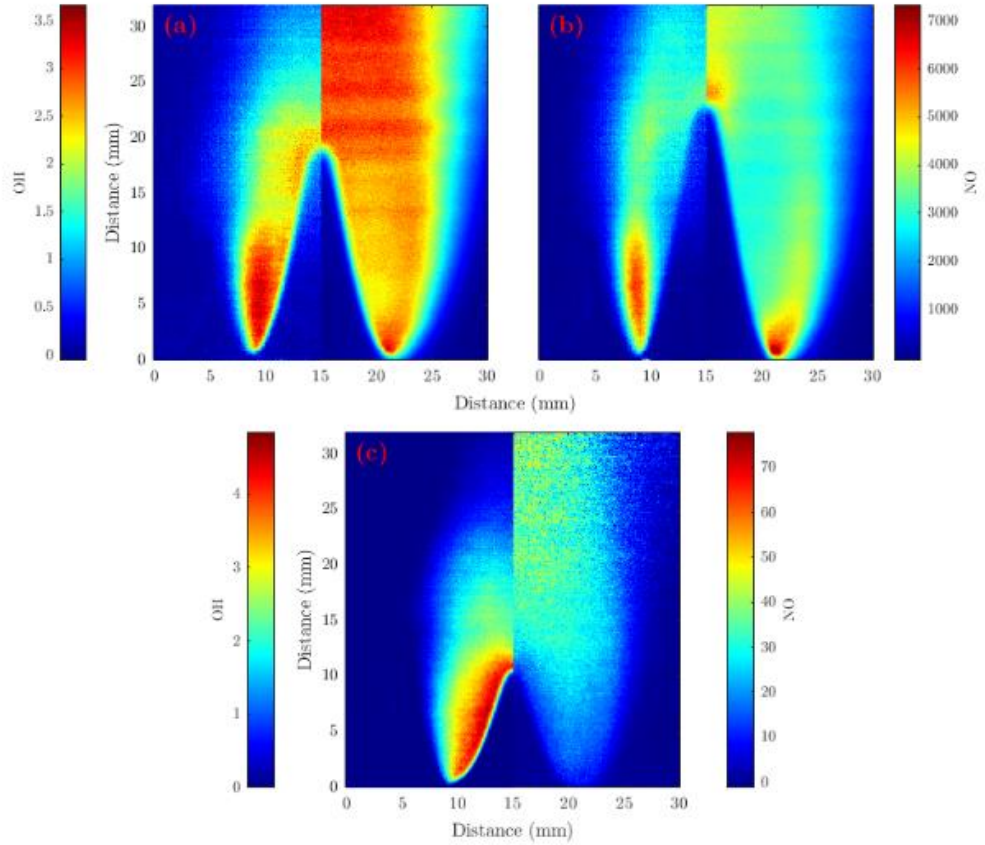

Fig. 2. Corrected OH-PLIF (left) and NO-PLIF (right) images for the two 65/35 (v/v) NH_3/H_2 flames, (a) lean and (b) rich, and the (c) reference CH_4 lean flame. The [OH] and [NO] scales are the same for the (a) and (b) and are shown on the left and right respectfully.

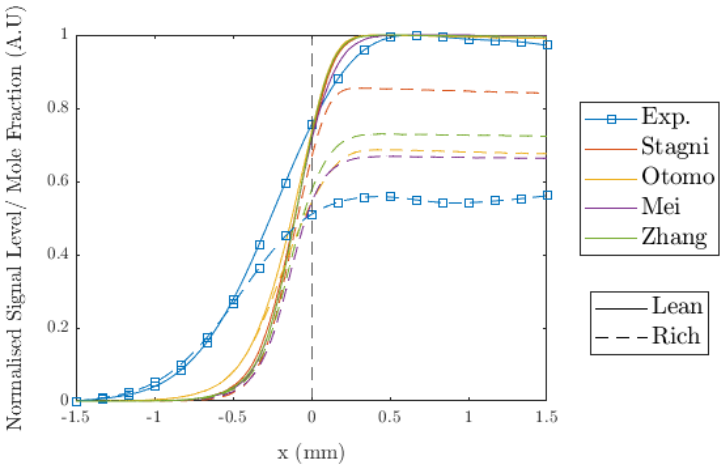

Fig. 3. Experimental and computed NO 1D line profiles for the two 65/35 (v/v) NH_3/H_2 flames. Each profile is normalised using the maximum of its corresponding lean case.

the existence of a secondary flame in the rich flame, which can be seen in the corresponding OH-PLIF portion of Fig. 2b. A secondary flame is formed on the outside of the rich flame due to fuel re-burn with the surrounding air, as it is not all consumed through the primary reaction zone, therefore there will be more fuel-NO formed there as a result.

It is also clear from Fig. 2 that neither of the NH_3/H_2 flames obtained a similar burning velocity to the reference methane flame. Due to the flames having similar bulk velocities of reactants, the burning velocities are comparable by flame height or cone angle. The methane flame has a lower flame height and larger cone angle, therefore a higher burner

velocity. This is in line with the NH_3/H_2 flame speed results presented by Zhang et al. [4] and methane flame speed results compiled by Pizzuti et al. [39].

The normalised NO line profiles for the lean and rich 65/35 (v/v) NH_3/H_2 flames are presented in Fig. 3. It can be seen that an increase in equivalence ratio (from lean to rich) causes a decrease in maximum relative NO level for both the experimental and computed profiles (at constant adiabatic flame temperature). This would be expected as the dominant production pathway for NO in ammonia flames is the HNO intermediate channel, which is primarily served by the O/OH radical pool [1]. Thus, the higher air content in the lean flame will produce a higher concentration of O/OH radicals leading to higher concentrations of NO. Furthermore, as can be seen in the next section, Fig. 4, the increase in NH_2 with an increase in equivalence ratio will also lead to the reduction of NO production in the rich flame. NH_2 has been shown to cause a substantial reduction in NO through the reactions NH2 + NO↔NNH + OH and NH2 + NO↔H2 O + N2 [40,41].

When comparing the different computational profiles, it can be observed that the Mei mechanism most closely reflects the relative reduction in experimental NO intensity from lean to rich. The experimental results show a ≈44% reduction in NO signal intensity, while the Mei mechanism estimates a ≈37% reduction. For comparison only a ≈15% reduction is estimated by the Stagni mechanism. The experimental results also show a much earlier formation, relative to the flame front, than the computed results. The experimental NO profiles start increasing from up to around 1.5 mm before the flame front, whereas all of the computed profiles start increasing around 0.75 mm before the flame front. The Otomo mechanism is the only one to show any notable difference in starting point compared to the other computed profiles, up to 1 mm before the flame front. This suggests that the mechanisms both overestimate the spatial formation rates of NO and underestimate the distance that it starts forming before the flame front. Furthermore, this highlights the inaccuracies in the modelling of low temperature ammonia breakdown and NO formation, as well as the effect of pyrolysis, in these mechanisms, which need to be studied in further detail.

Characteristics of Chemiluminescence Profiles

Figures 4a and 4b show the normalized NH* (experimental) and NH (computed) line profiles for the lean and rich 65/35 (v/v) NH_3/H_2 flames and their integrals respectively. All the integrals are evaluated over the same domain as the profiles, ±1.5 mm from their respective zero-reference points. It is clear from Fig. 4b that an increase in equivalence ratio increases the production of NH*, for the same

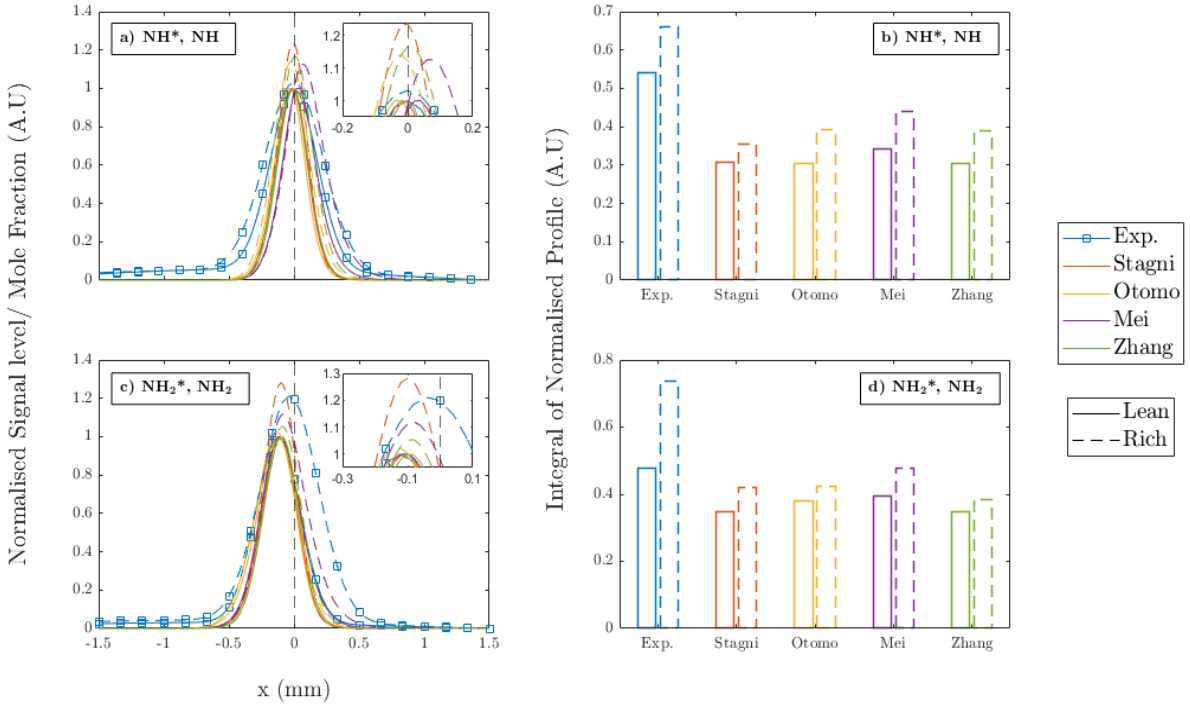

Fig. 4. Normalised 1D line profiles for experimental/computed (a) NH* and NH and (c) NH_2* and NH_2 results as well as (b,d) being their respective integrals over the same domain for the lean and rich cases for 65/35 (v/v) NH_3/H_2. The lean flame profiles are normalised using their own maximum values and rich flame profiles are normalised using their respective lean case maximum values.

adiabatic flame temperature. The trend is consistent for both the experimental NH* and computed NH profiles. This is expected, as the primary pathway for NH production is the breakdown of NH_2. NH_2 is directly proportional to the NH_3 fraction in the fuel and its primary reducers are H and OH radicals [1]. Hence, it can be assumed that NH production is most dependent on H radical concentration in NH_3/H_2 flames, since OH radical concentration decreases with an increase in equivalence ratio (seen in Figs. 2a/b and 5b). Therefore, it would be expected that an increase in the hydrogen fraction of the fuel would also cause an increase NH production, assuming H radical levels are directly proportional to the level of H_2 in the fuel.

Furthermore, it can be observed in Fig. 4b that the integrals of the normalized NH* and NH profiles are larger for the experimental results than the computed. This difference is primarily due to having a larger profile width, which can be seen in Fig. 4a. However, the percentage difference between the lean and rich integrals are actually larger for the Otomo, Mei and Zhang mechanisms with 29.2, 29.5 and 27.8% increase, respectively. This is compared to 22% for the experimental results, whilst the Stagni mechanism only shows a 14.9% increase. This shows that, in terms of relative NH production between slightly lean and rich flames with the same adiabatic flame temperature, the mechanisms mostly predict the difference in NH production quite well.

The normalized NH_2* (experimental) and NH_2 (computed) line profiles for the lean and rich 65/35 (v/v) NH_3/H_2 flames and their integrals are shown in Figs. 4c and 4d, respectively. All the experimental and computational NH_2* and NH_2 results show the same trend that an increase in equivalence ratio increases the production of NH_2. Similarly to NH, the primary reducers are H and OH radicals, and as OH levels decrease with an increase in equivalence ratio, it can be assumed that H radicals play the dominant role in the reduction of NH_2 [1].

In terms of spatial distribution of NH_2* and NH_2, it can be seen from Fig. 4c that it generally starts forming well before the flame front. All the profiles, except the rich test condition, seem to peak between 80-120 μm before the flame front. NH_2 is formed as a direct result of breakdown of the NH_3 in the fuel, which starts to occur well before higher temperatures are reached at the flame front. In jet-stirred reactor experiments it has been shown to decompose from around 1,000 K [4,19], which is significantly lower compared to the adiabatic flame temperatures of the test conditions in this study.

The experimental NH_2* results show a much greater percentage increase from lean to rich than estimated by the reaction mechanisms for NH_2 (Figs. 4c and 4d). The experimental normalized profile integrals show an increase of 54.1% from lean to rich compared to only 21.4, 11.4, 21.3 and 10.6% for the Stagni, Otomo, Mei and Zhang mechanisms, respectively. This large difference would suggest that the mechanisms underestimate the amount of NH_2 formation in these flames. However, it is also likely that NH_2* would undergo the most quenching as it is the first intermediate to be formed from the breakdown of NH_3. Furthermore, the integrals are also larger than their computed counterparts, similar to the NH results. This would suggest that, along with the [NO] forming much earlier than the computed NO, all of the mechanisms underestimate the width of the reaction zone in 65/35 (v/v) NH_3/H_2 flames.

Comparison of Chemiluminescence Markers to Computed Heat Release Rate

Figures 5a and 5b show the normalized experimental NH* and OH* profiles respectively. Their peaks line up well with the flame front (maximum [OH] gradient) for both the lean and rich 65/35 (v/v) NH_3/H_2 conditions investigated in this study. Figure 5c shows the integrals of the lean and rich normalized profiles for NH*, OH* and the computed HRR values for each mechanism. Similar to the experimental results, the computed HRR profiles are normalized using their lean case maximum before being integrated over the same domain. From Fig. 5c it is clear that an increase in equivalence ratio, but with the same adiabatic flame temperature at the test conditions, results in an increase in overall level for all the computed HRRs and the experimental NH*. However, OH* levels show the opposite trend. These trends have previously been discussed for NH and OH in previous sections, but in terms of HRR this is expected due to the higher fuel percentage of the reactants resulting in a higher amount of energy release. This illustrates the potential suitability of using NH* chemiluminescence as both a marker and for direct measurement of HRR in NH_3/H_2 flames. However, further experimentation with a wider range of equivalence ratios and NH_3/H_2 mixture compositions would need to be tested to confirm this.

Figure 6 shows the normalised computed NH and OH gradient profiles, with the zero-reference point on the x-axis being the respective point of maximum HRR. As previously explained, the experimental profiles are shifted based on their maximum [OH] gradient and computed profiles shifted based on their maximum HRR values. Therefore, Fig. 6 allows for a better comparison between computed and experimental profile alignment by showing how the computed NH, OH gradient and maximum HRR compare. The maximum computed HRR and NH

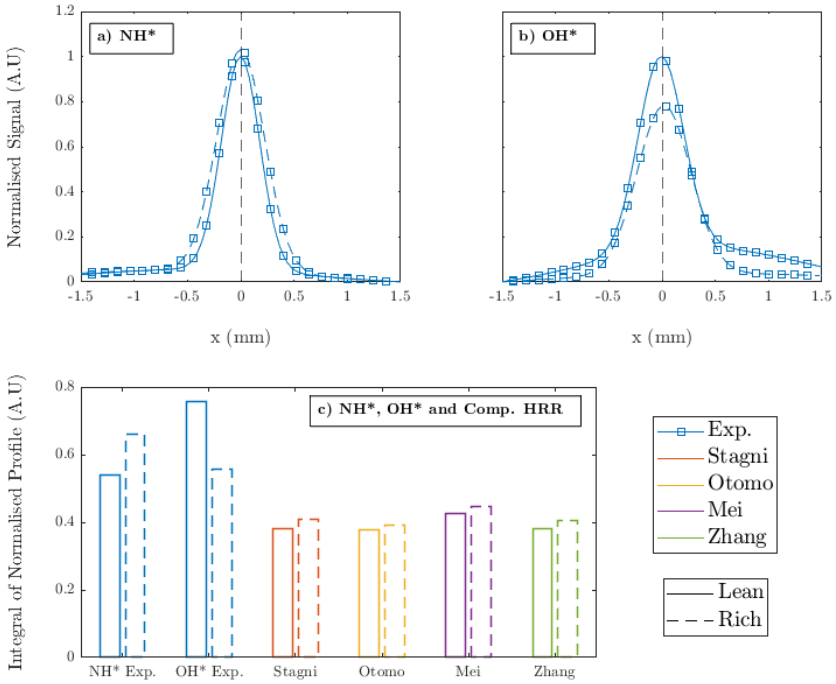

Fig. 5. Normalised 1D line profiles for experimental (a) NH* and (b) OH* results as well as (c) their integrals and HHRs computed for each mechanism for the lean and rich cases using 65/35 (v/v) NH_3/H_2. The lean flame profiles are normalised using their own maximum values and rich flame profiles are normalised using their respective lean case maximum values.

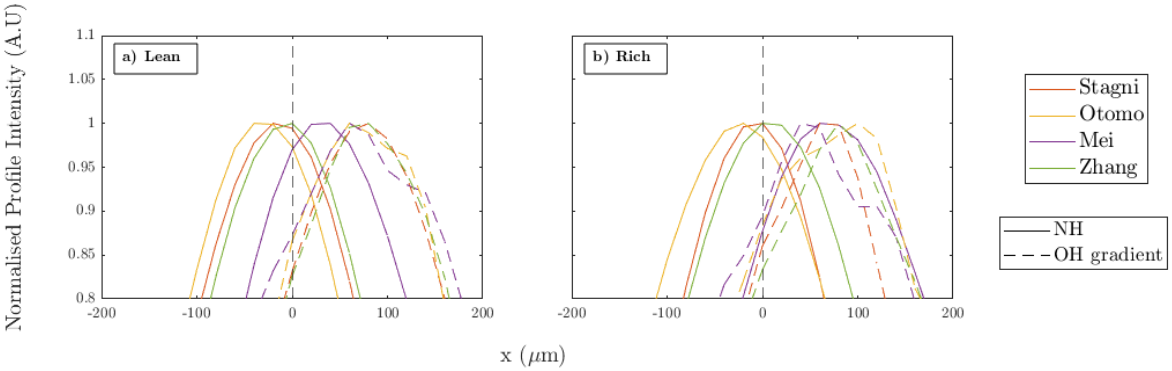

Fig. 6. Normalised 1-D line profiles for computed NH and OH gradient for the (a) lean and (b) rich 65/35 (v/v) NH_3/H_2 flames. All profiles are normalised using their own maximum.

peak line up quite well for all the mechanisms besides the Mei mechanism for both the lean and the rich cases. The Zhang mechanism shows the most accurate alignment, while the Stagni aligned well for the rich but is offset by around -20 μm for the lean. The Otomo and Mei NH profiles are both offset for the lean and rich. For Otomo by around -40 and -20 μm, respectively whilst for Mei it is by around +40 and +60 μm, respectively. Now comparing the relative position between the NH peaks and OH gradient peaks, they are all offset by between 80-100 μm except for the Mei mechanism. The Mei mechanism NH peaks seem to show much better alignment with the OH gradient peaks than the maximum HRR, especially for the rich case. The OH gradient and NH peaks line up after the point of maximum HRR by around 60-80 μm for the Mei mechanism. Therefore, in terms of flame structure, the Mei mechanism is the most comparable to the experimental results obtained due to the OH gradient alignment (which is how the experimental results are all aligned in Figs. 3, 4a, 4c, 5a and 5b). Although, in terms of using maximum [OH] gradient as an experimental HRR marker for NH_3/H_2 flames, the computational results would suggest that this is not very accurate, and that [NH] or NH* would be better

suited. On the other hand, the experimental results show that NH*, OH* and [OH] gradient all line up well for the test conditions in this study. Therefore, this would also suggest that the mechanisms are not accurately predicting both the spatial formation rates of OH and the spatial distribution of the HRR.

Conclusions

Simultaneous OH/NO-PLIF and OH-PLIF/Chemiluminescence imaging was performed on NH_3/H_2 flames for the first time in a simple Bunsen burner configuration. Maximum [OH] gradient was used as a reference point to compare the spatial distribution of NO, NH*, NH_2* and OH*. Both OH* and NH* showed a good spatial correlation with the maximum [OH] gradient.

Computational one-dimensional flame analysis was conducted using the same parameters as the experimental campaign and compared to the experimental results. Four different mechanisms were chosen from literature that have been used to simulate NH_3/H_2 flames. The NH* signal levels show a positive correlation to the level of computed heat release, which indicates that it has potential to be used as a direct HRR measurement species in NH_3/H_2 flames. Their application as experimental flame front markers in NH_3/H_2 should be investigated further to include a wide range of equivalence ratios and NH_3/H_2 ratios.

In terms of spatial and total species formation compared to the experimental results and correlation with flame front/HRR, the mechanism developed by Mei et al. [17] showed the closest comparable trends. However, all the mechanisms underestimated the relative increase in NH_2 level from lean to rich by >30%, although this could be due to high levels of NH_2* quenching. Furthermore, it seems as though all the mechanisms underestimate the width of the reaction zone of 65/35 (v/v) NH_3/H_2 flames, as all of the experimental 1-D line profiles have a greater width/integral value than their computed counterparts.

Acknowledgments

The authors would like to acknowledge EPSRC (EP/T009314/1) and UKRI (MR/T019735/1) for their support towards this work.

Conflicts of Interest

The authors declare no conflict of interest.

References

1. Kobayashi H, Hayakawa A, Somarathne K, Okafor EC. Science and technology of ammonia combustion. *Proc Combust Inst*. 2019; 37(1): 109-133. doi: https://doi.org/10.1016/j.proci.2018.09.029.

2. Valera-Medina A, Pugh, DG, Marsh R, Bulat G, Bowen P. Preliminary study on lean premixed combustion of ammonia-hydrogen for swirling gas turbine combustors. *Int J Hydrogen Energy*. 2017; 42(38):24495-24503. doi: https://doi.org/10.1016/j.ijhydene.2017.08.028.

3. Hussein N, Valera-Medina A, Alsaegh A. Ammonia- hydrogen combustion in a swirl burner with reduction of NOx emissions. *Energy Procedia*. 2019;158:2305-2310. doi: https://doi.org/10.1016/j.egypro.2019.01.265.

4. Zhang X, Moosakutty S, Rajan R, Younes MSarathy S. Combustion chemistry of ammonia/hydrogen mixtures: Jet-stirred reactor measurements and comprehensive kinetic modeling. *Combust Flame*. 2021; 234: 111-653. doi: https://doi.org/10.1016/j.combustflame.2021.111653.

5. Valera-Medina A, Xiao H, Owen-Jones M, David W, Bowen P. Ammonia for power. *Prog Energy Combust Sci.* 2018; 69: 63–102. doi: https://doi.org/10.1016/j.pecs.2018.07.001.

6. Valera-Medina A, Gutesa M, Xiao H, Pugh D, Giles A, Goktepe B, Marsh R, Bowen P. Premixed ammonia/hydrogen swirl combustion under rich fuel conditions for gas turbines operation. *Int J Hydrogen Energy*. 2019; 44(16): 8615–8626. doi: https://doi.org/10.1016/j.ijhydene.2019.02.041.

7. Lhuillier C, Brequigny P, Contino F, Mounaïm-Rousselle C. Experimental study on ammonia/hydrogen/air combustion in spark ignition engine conditions. *Fuel*. 2020; 269: 117-448. doi: https://doi.org/10.1016/j.fuel.2020.117448.

8. Koike M, Suzuoki T. In-line adsorption system for reducing cold-start ammonia emissions from engines fueled with ammonia and hydrogen. *Int J Hydrogen Energy*. 2019; 44(60):32271–32279. doi: https://doi.org/10.1016/j.ijhydene.2019.10.105.

9. Comotti M, Frigo S. Hydrogen generation system for ammonia-hydrogen fuelled internal combustion engines. *Int J Hydrogen Energy*. 2015; 40(33): 10673–10686. doi: https://doi.org/10.1016/j.ijhydene.2015.06.080.

10. Otomo J, Koshi M, Mitsumori T, Iwasaki H, Yamada K. Chemical kinetic modelling of ammonia oxidation with improved reaction mechanism for ammonia/air and ammonia/hydrogen/air combustion. *Int J Hydrogen Energy*. 2018; 43(5): 3004–3014. doi: https://doi.org/10.1016/j.ijhydene.2017.12.066.

11. Zhang H, Han X, Jiang J, Li X, Gan X, Zhou B. Numerical study of experimental feasible heat release rate markers for NH_3–H_2-air pre-mixed flames. *Int J Hydrogen Energy*. 2022; 47(65): 28165–28175. doi: https://doi.org/10.1016/j.ijhydene.2022.06.124.

12. Bioche K, Bricteux L, Bertolino A, Parente A, Blondeau J. Large Eddy Simulation of rich ammonia/hydrogen/air combustion in a gas turbine burner. *Int J Hydrogen Energy*. 2021; 46(79): 39548–39562. doi: https://doi.org/10.1016/j.ijhydene.2021.09.164.
13. Hussein N. Ammonia Cracking with Heat Transfer Improvement Technology. PhD Thesis, Cardiff University, Cardiff, Wales. 2019.
14. Zhu X, Khateeb A, Guiberti T, Roberts W. NO and OH* emission characteristics of very-lean to stoichiometric ammonia-hydrogen-air swirl flames. *Proc Combust Inst*. 2021; 38(4):5155–5162. doi: https://doi.org/10.1016/j.proci.2020.06.275.
15. Mashruk S, Okafor E, Kovaleva M, Alnasif A, Pugh D, Hayakawa A, Valera-Medina A. Evolution of N2O production at lean combustion condition in NH3/H2/air premixed swirling flames. *Combust Flame*. 2022; 244: 112-299. doi: https://doi.org/10.1016/j.combustflame.2022.112299.
16. Song Y, Hashemi H, Christensen J, Zou C, Marshall P, Glarborg P. Ammonia oxidation at high pressure and intermediate temperatures. *Fuel*. 2016; 181: 358–365. doi: https://doi.org/10.1016/j.fuel.2016.04.100.
17. Mei B, Zhang J, Shi X, Xi Z, Li Y. Enhancement of ammonia combustion with partial fuel cracking strategy: Laminar flame propagation and kinetic modeling investigation of $NH_3/H_2/N_2$/air mixtures up to 10 atm. *Combust Flame*. 2021; 231:111-472. doi: https://doi.org/10.1016/j.combustflame.2021.111472.
18. Mei B, Ma S, Zhang Y, Zhang X, Li W, Li Y. Exploration on laminar flame propagation of ammonia and syngas mixtures up to 10 atm. *Combust Flame*. 2020; 220: 368–377. doi: https://doi.org/10.1016/j.combustflame.2020.07.011.
19. Stagni A, Cavallotti C, Arunthanayothin S, Song Y, Herbinet O, Battin-Leclerc F, Faravelli T. An experimental, theoretical and kinetic-modeling study of the gas-phase oxidation of ammonia. *Reaction Chem Eng*. 2020; 5(4): 696–711. doi: https://doi.org/10.1039/c9re00429g.
20. Mulla I, Godard G, Cabot G, Grisch F, Renou B. Quantitative imaging of nitric oxide concentration in a turbulent n-heptane spray flame. *Combust Flame*. 2019; 203: 217–229. doi: https://doi.org/10.1016/j.combustflame.2019.02.005.
21. Mulla I, Godard G, Renou B. Instantaneous planar measurements of nitric oxide concentration in a turbulent n-heptane spray flame. *Combust Flame*. 2019; 208: 451–471. doi: https://doi.org/10.1016/j.combustflame.2019.07.026.
22. Bohon M, Guiberti T, Roberts W. PLIF measurements of non-thermal NO concentrations in alcohol and alkane premixed flames. *Combust Flame*. 2018; 194: 363–375. doi: https://doi.org/10.1016/j.combustflame.2018.05.024.
23. Fan Q, Liu X, Cai X, Brackmann C, Alden M, Bai X, Li Z. Structure and scalar correlation of ammonia / air turbulent premixed flames in the distributed reaction zone regime. *Combust Flame*. 2022; 241: 112090 doi: https://doi.org/10.1016/j.combustflame.2022.112090.
24. Rocha R, Zhong S, Xu L, Bai X, Costa M, Cai X, Kim H, Brackmann C, Li Z, Alden M. Structure and laminar flame speed of an ammonia/methane/air premixed flame under varying pressure and equivalence ratio. *Energy Fuels*. 2021; 35(9): 7179–7192. doi: https://doi.org/10.1021/acs.energyfuels.0c03520.
25. Versailles P, Durocher A, Bourque G, Bergthorson J. Nitric oxide formation in lean, methane-air stagnation flames at supra-atmospheric pressures. Proc Combust Inst. 2019; 37(1):711–718. doi: https://doi.org/10.1016/j.proci.2018.05.060.
26. Mashruk S, Marsh R, Runyon J, Morris S, Bowen P. Methodology and comparison of quantitative NO-LIF imaging in a bunsen burner with numerical simulation results. Int Symp Appl Laser Imag Tech Fluid Mech. Volume 19. 2018.
27. Mulla I, Dowlut A, Hussain T, Nikolaou Z, Chakravarthy S, Swaminathan N, Balachandran R. Heat release rate estimation in laminar premixed flames using laser-induced fluorescence of CH_2O and H-atom. *Combust Flame*. 2016: 165: 373–383. doi: https://doi.org/10.1016/j.combustflame.2015.12.023.
28. Ayoola B, Balachandran R, Frank J, Mastorakos E, Kaminski C. Spatially resolved heat release rate measurements in turbulent premixed flames. *Combust Flame*. 2006; 144: 1–16. doi: https://doi.org/10.1016/j.combustflame.2005.06.005.
29. Hu Y, Tan J, Lv L, Li X. Investigations on quantitative measurement of heat release rate using chemiluminescence in premixed methane-air flames. *Acta Astronautica*. 2019; 164: 277–286. doi: https://doi.org/10.1016/j.actaastro.2019.07.019.
30. Cheng M, Wang H, Xiao H, Luo K, Fan J. Emission characteristics and heat release rate surrogates for ammonia premixed laminar flames. *Int J Hydrogen Energy*. 2021; 46(24): 13461-13470. doi: https://doi.org/10.1016/j.ijhydene.2021.01.154.
31. Brackmann C, Alekseev V, Zhou B, Nordström E, Bengtsson P, Li Z, Alden M, Konnov A. Structure of premixed ammonia + air flames at atmospheric pressure: Laser diagnostics and kinetic modeling.

Combust Flame. 2016; 163: 370–381. doi: https://doi.org/10.1016/j.combustflame.2015.10.012.

32. Zeldovich YB. Oxidation of Nitrogen in Combustion. *Acta Physicochem*. 1946; 21: 577–628.

33. Glarborg P, Miller J, Ruscic B, Klippenstein S. Modeling nitrogen chemistry in combustion. *Prog Energy Combust Sci*. 2018; 67: 31–68. doi: https://doi.org/10.1016/j.pecs.2018.01.002.

34. Vignesh R, Ashok B. Critical interpretative review on current outlook and prospects of selective catalytic reduction system for De-NOx strategy in compression ignition engine. *Fuel*. 2020; 276: 117-996. doi: https://doi.org/10.1016/j.fuel.2020.117996.

35. Miller J, Bowman C. Mechanism and Modeling of Nitrogen Chemistry in Combustion. *Prog Energy Combust Sci*. 1989; 15(4):287–338. doi: https://doi.org/10.1007/0-387-32153-5_7.

36. Cormack AM. Representation of a function by its line integrals, with some radiological applications. *J Appl Physics*. 1963; 34: 2722–2727. doi: https://doi.org/10.1063/1.1729798.

37. Firman. 2D Abel Inversion. 2022. Online. Access: https://www.mathworks.com/matlabcentral/fileexchange/60271-2d-abel-inversion (visited on 06/21/2022).

38. Rotexo GmbH Co. Cosilab. Version 4.1.7. Online. Access: https://www.rotexo.com/index.php/en/.

39. Pizzuti L, Martins C, Dos Santos L, Guerra D. Laminar Burning Velocity of Methane/Air Mixtures and Flame Propagation Speed Close to the Chamber Wall. *Energy Procedia*. 2017; 120: 126-133. doi: https://doi.org/10.1016/j.egypro.2017.07.145.

40. Pugh D, Bowen P, Valera-Medina A, Giles A, Runyon J, Marsh R. Influence of steam addition and elevated ambient conditions on NOx reduction in a staged premixed swirling NH_3/H_2 flame. *Proc Combust Inst.* 2019; 37(4): 5401-5409. doi: https://doi.org/10.1016/j.proci.2018.07.091.

41. Mashruk S, Xiao H, Valera-Medina A. Rich-Quench-Lean model comparison for the clean use of humidified ammonia/hydrogen combustion systems. *Int J Hydrogen Energy*. 2021; 46(5): 4472-4484. doi: https://doi.org/10.1016/j.ijhydene.2020.10.204